Article

Kilowatt-scale solar hydrogen production system using a concentrated integrated photoelectrochemical device

Isaac Holmes-Gentle [1,3], Saurabh Tembhurne [1,2,3], Clemens Suter [1] & Sophia Haussener [1] ✉

The production of synthetic fuels and chemicals from solar energy and abundant reagents offers a promising pathway to a sustainable fuel economy and chemical industry. For the production of hydrogen, photoelectrochemical or integrated photovoltaic and electrolysis devices have demonstrated outstanding performance at the lab scale, but there remains a lack of larger-scale on-sun demonstrations (>100 W). Here we present the successful scaling of a thermally integrated photoelectrochemical device—utilizing concentrated solar irradiation— to a kW-scale pilot plant capable of co-generation of hydrogen and heat. A solar-to-hydrogen device-level efficiency of greater than 20% at an H_2 production rate of >2.0 kW (>0.8 g min^{-1}) is achieved. A validated model-based optimization highlights the dominant energetic losses and predicts straightforward strategies to improve the system-level efficiency of >5.5% towards the device-level efficiency. We identify solutions to the key technological challenges, control and operation strategies and discuss the future outlook of this emerging technology.

The efficient conversion of solar energy to fuel and chemical commodities offers an alternative to the unsustainable use of fossil fuels, where photoelectrochemical production of hydrogen has been identified as a promising route[1,2]. At present, solar fuel technologies are typically restricted to small-scale demonstrations (<100 W output power), for designs such as integrated photovoltaic (PV) plus electrolyser (EC)[3–8], photoelectrochemical cells (PEC)[9,10], photoparticulate systems[11,12] or thermochemical redox cycles[13]. To enable wide-scale implementation and use, it is imperative that pilot-scale on-sun demonstrations of solar fuel technologies are constructed to study and demonstrate scale-up feasibility[14–17]. However, there are multiple challenges to be overcome when scaling PEC or integrated PV + EC devices, which can depend on the specific device design, experimental configuration and materials used[18,19]. These challenges typically involve the often-competing requirements of high efficiency, high production rates, long-term stability, low cost and high sustainability. To illustrate how device specific

these challenges can be, photoparticulate systems can suffer from low efficiency and selectivity but could be deployed in inexpensive polyethylene tubes/bags[20] whereas III–V semiconductor and noble metal catalysts can be expensive but lead to efficient devices[21]. Therefore, the challenges of scaling solar fuel systems are non-trivial but broadly can be achieved by increasing photoabsorber area per device, increasing the number of devices deployed and/or through solar concentration[18]. In particular, solar concentration has been shown to be a promising route towards economically competitive, high-power-density devices permitting the use of more expensive photoabsorber materials[22–26]. The potential advantage of solar concentration is multifold as it also has the potential to improve the device efficiency[26] while simultaneously co-generating useful heat[2,3,27].

Thermally integrated photovoltaic plus electrolyser designs utilizing concentrated solar have been shown to take advantage of optimized thermal management and, therefore, exhibit exceptional

[1]Laboratory of Renewable Energy Science and Engineering, EPFL, Lausanne, Switzerland. [2]SoHHytec SA, EPFL Innovation Park, Batiment C, Lausanne, Switzerland. [3]These authors contributed equally: Isaac Holmes-Gentle and Saurabh Tembhurne. ✉e-mail: sophia.haussener@epfl.ch

performance characteristics. Specifically, thermal management allows for the synergistic effect of combined photoabsorber cooling and reduced electron-hole recombination with reactant and catalyst heating and reduced overpotentials[3–8]. Furthermore, solar fuel systems capable of co-generation of products (for example, fuel, electricity and heat) have received recent interest[28,29] due to the increased system efficiency. However, previous demonstrations of this technology are somewhat limited in H_2 production power (<32 W output power based on the higher heating value (HHV)), and only some devices were tested under real-world solar conditions[4,5,8]. In addition to the potential improvements in catalysis and membrane conductivity (within material and operational limits)[30], a further advantage of thermal integration is that the external heat often required to operate compact electrolyser systems[31] can be provided by unavoidable thermal recombination in the concentrator photovoltaic (CPV) module. This removes an additional heater from the balance of plant, which is otherwise required for compact polymer electrolyte membrane (PEM) stacks[31].

In previous work, a lab-scale integrated PEC device has been experimentally demonstrated under 474 kW m^{-2} irradiance from a high-flux solar simulator[3] and achieved a >15% solar-to-hydrogen (STH) efficiency at a 32 W hydrogen power output. A similar integrated architecture, based on tandem junction III–V solar cells, has been proposed and built[4,8], and a scaled on-sun system based on eight modules demonstrated (90.7 cm^2 input light area × 8 modules, H_2 power ~ 13 W) (ref. [5]) and achieved a STH efficiency of 16.4% (19.8% HHV). Additionally, this direct-integration device architecture has also been applied to developing technologies such as alkaline anion exchange membrane electrolysis[7]. These experimental demonstrations, along with the previous modelling[27,30,32,33], demonstrate the synergistic effect of heat integration of the photoelectrochemical device. However, these studies also established the need for careful thermal management to advantageously benefit from such thermal integration, highlighting the integrated device design, selected operating conditions and the observation of material limits (for example, PV, PEM) as key issues. Direct electrical connection and thermal integration gives rise to some non-trivial coupled effects that have previously been studied theoretically[27,30], where flow-rate control can adjust the device operating point to advantageously mitigate degradation effects or variation in irradiation conditions[30]. Dynamic effects of the coupled system were also simulated and key control challenges identified, such as the effect of component failure[27], which had to be addressed in this experimental work.

Here we present a scaled prototype of a solar hydrogen and heat co-generation system utilizing concentrated sunlight operating at substantial hydrogen production rates. Building on the design of the laboratory-scale demonstration[3], the polymer electrolyte membrane electrolyser (selected as it is the pre-eminent electrolysis technology for integration into intermittent renewable energy systems[34–36]) is coupled to a concentrated PV module through the common deionized water stream to achieve close thermal integration. This configuration is advantageous as it permits the use of state-of-the-art commercial components that have been demonstrated at a high technology-readiness level.

System overview

The solar energy to the hydrogen, oxygen and heat co-generation system demonstrated here is shown in Fig. 1, and the design, construction and control are detailed further in the Methods. Solar light is concentrated by a dual-axis tracking parabolic dish concentrator to a solar reactor which comprises a shield, aperture with flux homogenizer and triple-junction III–V PV module, proton exchange membrane EC stack embedded in the reactor unit and water pump (to recycle over the PV). A technical illustration of the integrated photoelectrochemical (IPEC) reactor unit is shown in Fig. 1b, where the PV module and EC stacks are housed inside.

Given the novelty and pilot scale of the demonstrator, numerous non-trivial design and operational challenges had to be overcome, as detailed further in Supplementary Note 1. Notably, the two-pump design (that is, global and PV recycle) proposed here decouples the conflicting water flow-rate requirements of the PV and EC so that satisfactory heat transfer can be achieved in the CPV heat exchanger while simultaneously controlling the overall water temperature increase over the CPV module and stoichiometric water ratio in the EC. Furthermore, due to the pilot-scale nature of the system, the solar dish size is not optimized to the reactor size and therefore an additional water-cooled shield is required to absorb the excess concentrated light. This shield could be replaced with a larger-area homogenizer/concentrated PV unit and passively cooled shield in future work, further reducing the complexity of design.

Experimental results and performance

The complete system was operated over a period of more than 13 days in August 2020 and February/March 2021, and the key measured variables are shown in Fig. 2 and Supplementary Fig. 8. Operation under different environmental conditions was demonstrated where the ambient temperatures ranged from about 20 °C in August to about 8 °C in late February. The meteorological conditions also varied considerably over the time periods of operation as shown in the direct normal irradiance (DNI) data (Fig. 2a): for example, 19 August 2020–clear sky with scattered cumulus clouds; 20 August 2020–clear sky; 23 February 2021–homogeneous translucent upper-atmospheric clouds (for example, cirrostratus).

Figure 2b shows the instantaneous H_2 production rate that produced up to 0.9 Nm^3 hr^{-1} with a mean of 0.59 N m^3 hr^{-1} (49.7 g hr^{-1}) over the entire operation period (corresponding to EC current of I_{EC} = 41.3 A). This was calculated from the EC current assuming a high Faradaic efficiency of unity typical of PEM electrolysis and was confirmed with gas chromatography detailed in Supplementary Note 2. During operation of the integrated device, the global water flow rate was 4.92 l min^{-1} (which corresponds to a stoichiometric water ratio (λ) in the EC of λ = 460 at 60 A), and the PV recycle water flow rate was 10.3 l min^{-1}. The typical operating absolute pressures in the anodic stream is about 3.5 bar, the cathodic side is about 29 bar, and the H_2 storage tank pressure ranged from 1 to 31 bar (dependent on the state of the storage). Furthermore, system inlet and outlet water temperatures were typically 14.4 °C and 45.1 °C, respectively, and the reactor outlet temperature was typically 60–70 °C.

Shown in shown Fig. 3a, the instantaneous input and output powers for the 13-day experimental campaign can be integrated over the duration of the day to calculate daily averaged performance metrics. While solar-to-fuel efficiencies are typically based on the Gibbs free energy under standard conditions[37], it is common in the water electrolysis field for voltage efficiencies to be reported on an enthalpy basis (HHV)[34], and therefore both definitions (discussed further in Supplementary Note 4) will be used here for completeness. The overall system fuel efficiency based on the reaction enthalpy (higher heating value, 286 kJ mol^{-1}) and the overall system heat efficiency averaged over the entire operating duration was 6.6% ± 0.6% and 35.3%, respectively. Correspondingly, this system fuel efficiency is 5.5% ± 0.5% based on the Gibbs free energy (237 kJ mol^{-1}). The system efficiency is defined in Methods and includes the external electricity used for all auxiliary components (0.58 kW, detailed in Supplementary Fig. 8). The experimental uncertainty analysis is detailed further in Supplementary Note 5. While the fuel efficiency remained approximately constant, the heat efficiency decreases in the winter months when compared with the summer experimental campaign, probably due to increased heat loss due to cooler ambient temperatures.

As outlined in Supplementary Table 3, the maximal peak hydrogen production rate calculated over a 5 minute window was 14.0 Nl min^{-1} (1.26 g min^{-1}), and during the complete campaign, more
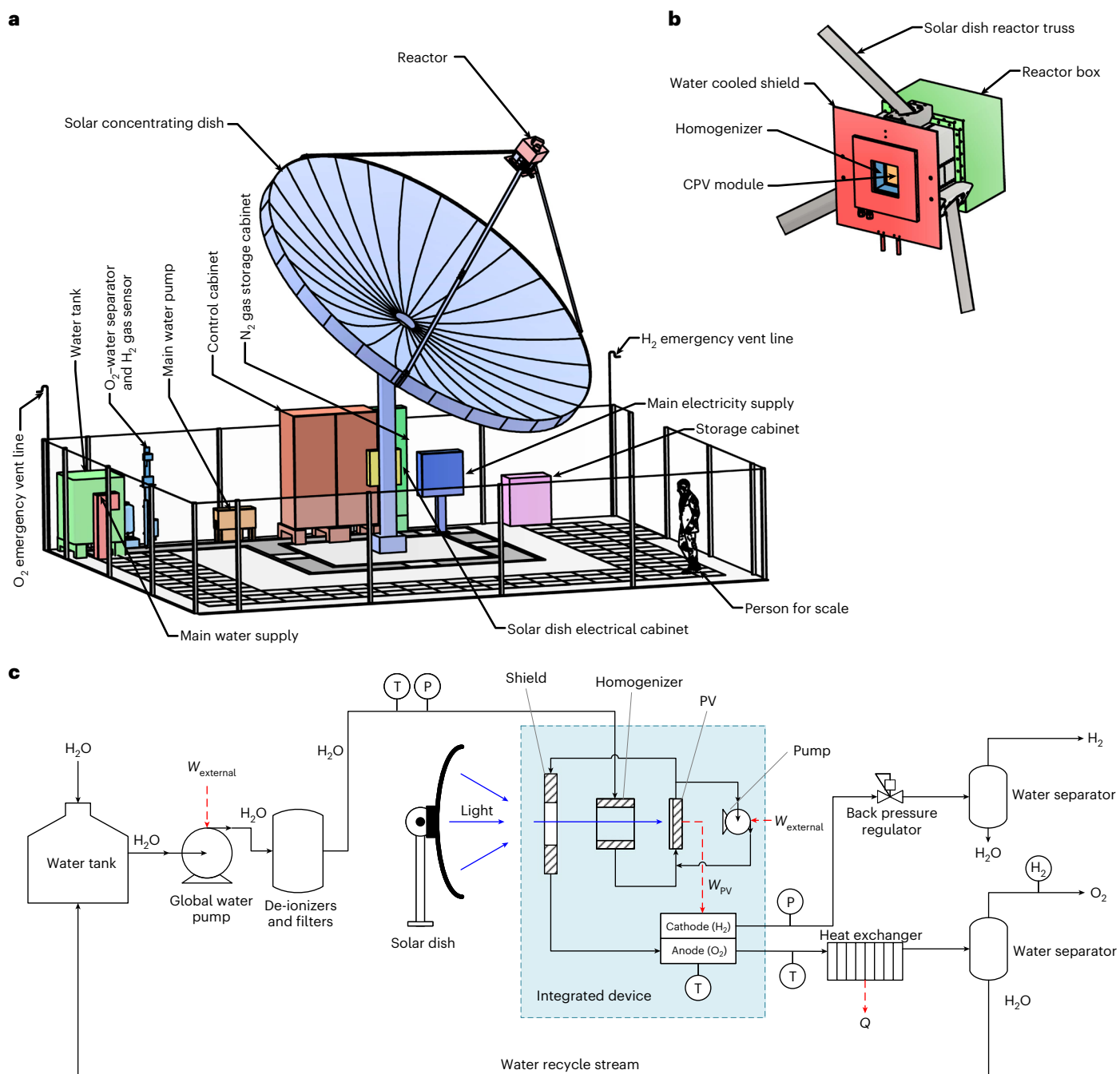
Fig. 1 | Overview of the system. a, Technical illustration of the overall site showing key components such as the solar parabolic concentrator dish, reactor and ancillary hardware and cabinets. **b**, Close-up of the integrated reactor showing the assembly of the shield, homogenizer, PV and enclosure. **c**, A simplified process and instrumentation diagram of the system showing material and energy flows. The key input/output/intermediate energy streams are composed of the PV-generated electrical work available for electrolysis, heat output from the heat exchanger and the external work required for water pumping. W and Q stands for work and heat respectively and sensors are denoted by a circle (T = temperature sensor, P = pressure sensor, H_2 = hydrogen concentration sensor). Photographs of the system can be found in Supplementary Fig. 1.

than 3.2 kg of solar hydrogen was produced. The system produces on average $10.6\ kW_{th}$ of thermal heat at an outlet temperature of 45.1 °C, as defined in Methods. The peak thermal output (during a 5 min period) was $14.9\ kW_{th}$, and a total $679\ kWh_{th}$ was produced during the 13 days operation. Notably, thermal integration was estimated to reduce the required auxiliary electrical demand by over half due to the removal of an auxiliary heater (estimated power: ~ 0.6 kW based on an EC electrical input of 3.1 kW and a heating to EC power ratio of ~ 20%, based on ref. 31). Furthermore, this thermal integration

removes the associated heater capital costs and simplifies the balance of the plant.

Due to compromises pertaining to the implementation at the pilot scale, a number of components are not optimized, leading to an appreciably lower system efficiency than achievable[27]. Specifically, the dish size is larger than necessitated by the reactor and so a large proportion of concentrated light is absorbed by the light shield. To facilitate experimental comparison with lab-scale thermally integrated PV–EC devices, a second diagnostic device efficiency can be defined as the
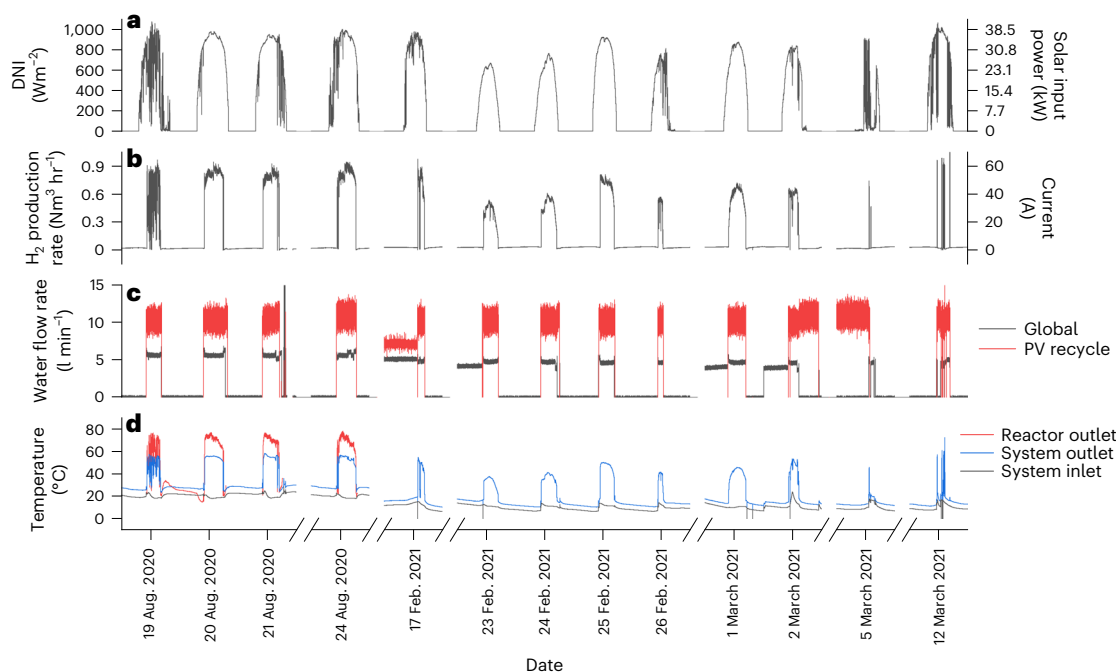
Fig. 2 | Temporal system performance over multiple days. a, Direct normal irradiance and solar input power (= DNI × A_{dish}) where A_{dish} is the total dish area. **b**, Hydrogen production rate (that is, left y axis), as calculated from electrolyser current (that is, right y axis), assuming Faradaic efficiency of unity as per discussion in Supplementary Note 2. A system operating current of 50 A corresponds to an EC current density of 1 A cm^{-2}. **c**, Water flow rates (global, m_g, and PV recycle, m_r, flow rates). **d**, Temperatures of the system inlet water and system outlet water/O_2 streams and reactor outlet (after the EC stack). Aug. stands for August and Feb. stands for February.

ratio of fuel power to the solar power incident on the reactor aperture, that is, the PV ($\eta_{IPEC} = Q_{fuel}/Q_{PV}$). The ratio of Q_{solar} to Q_{PV} is estimated from Lambertian flux target calibration (Supplementary Methods 1 for details) to be 27.5%. Finally, the mean diagnostic device efficiency based on enthalpy during operation achieved over the entire experimental campaign is calculated to be 24.4% ± 2.8% and when averaged over the best performing day equal to 27.2%. This corresponds to 20.3% ± 2.3% and 22.6%, respectively, when based on Gibbs free energy.

The STH efficiency for lab-scale PEC devices is typically calculated based on Gibbs free energy[37] in the same manner as the device-level fuel efficiency defined in this work and so can be compared on an equal basis. The average STH device-level efficiency achieved in this work (20.3%) is one of the highest when compared with all previous work (Supplementary Fig. 9) and notably compares well with previous devices employing thermal integration of PV and PEM EC components (5–18%) (refs. 3–5,7,8,38). Notably, a two order-of-magnitude increase in solar hydrogen production power (HHV) is achieved when compared with previous results: 32 W (ref. 3) vs >2.0 kW achieved in this work (averaged over total experimental time). Furthermore, this was achieved under real-world on-sun conditions (comparable to refs. 4,5,8), contrasting with the lab-scale solar-simulator demonstrations[3,7,38]. Efficiency improvements in this work are made through the use of state-of-the-art triple-junction photovoltaic materials and through an improved PV–EC coupling efficiency (which better matches the produced photovoltage to the requirements of the electrolyser stack). A performance comparison with the available literature for solar fuel technologies can be found in Supplementary Fig. 9. The demonstrated efficiencies achieved in this work compare well with recent large-scale STH demonstrations based on particulate PEC water splitting (0.76%, ~700 W output power)[14] or thermochemical syngas production (solar redox unit = 3.86%, system-level = 2.3%, ~300 W output power[16] and solar-to-syngas = 4.1%, ~500 W output power[17]).

Process variable correlations and steady-state simulation

Figure 3b–d shows correlations of instantaneous operating parameters where the data were filtered for steady state and de-noised as defined in Supplementary Fig. 10. As expected from previous modelling efforts[27], a relationship between the measured current and voltage operating point and outlet water temperature can clearly be observed in Fig. 3b: higher operating temperatures of the integrated device lead to lower overpotentials and lower operating voltages.

To investigate the system performance further, a detailed zero-dimensional model was constructed as outlined in Supplementary Note 8. A good fit to the experimental data was achieved as shown in Fig. 3b–d with parameters taken from optical or individual component performance experiments. Shown in Fig. 3c,d, the fuel and heat power both show an approximately linear correlation against DNI (Q_{fuel} [kW] = 3.1955 × DNI [kW m^{-2}] − 0.4963, R^2 = 0.9137 and $Q_{thermal}$ [kW] = 14.4998 × DNI [kW m^{-2}] − 0.6145, R^2 = 0.8649), in close agreement with the simulation results. For fuel power, this trend is expected as, due to the position of the operating point on the PV and EC curve, the PV performance dominates; short-circuit current of the PV is approximately linearly proportional to irradiance. However, the system underperforms the theoretical model at low DNI values, where these periods of low DNI during system operation (<500 W m^{-2}) were observed to correlate with increased cloud/haze cover. Therefore, as detailed in Supplementary Note 7, it was hypothesized that this phenomena is attributed to increased circumsolar radiation (caused by forward scattering of light) during periods of increased cloudiness, which is measured as DNI by a solar irradiance sensor (typical acceptance half angle of 2.5°) (ref. 39), but our solar dish and homogenizer can make only partial use of it (ideal acceptable angle = ~0.8°). The proportion of circumsolar-to-direct radiation has been shown to impact the shape of the flux distribution[40], and the secondary optics (that is, homogenizer) will be sensitive to this. Deviation from the linear fit for heat power at
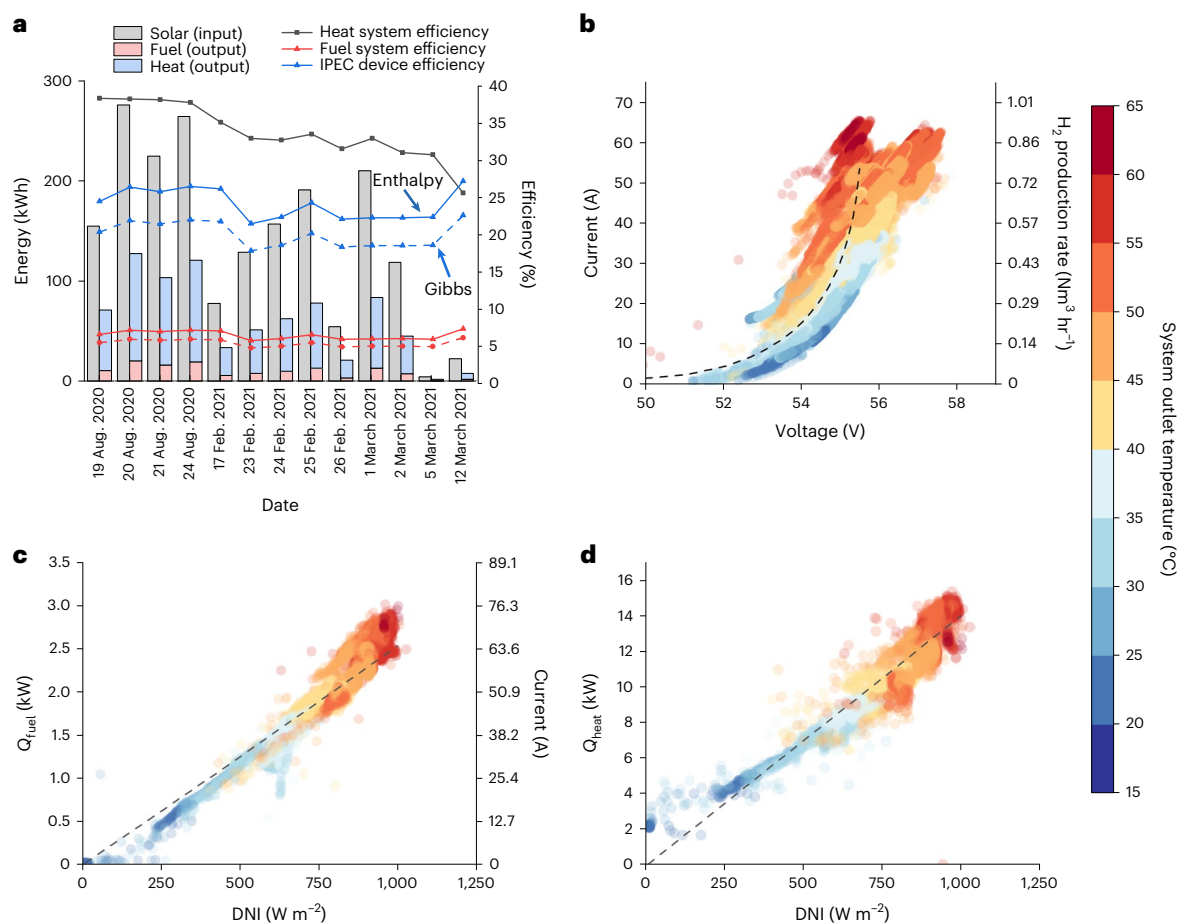
Fig. 3 | Averaged performance metrics and correlations from the experimental campaign. a, Daily performance metrics—input/output energy during operation and efficiencies. For the system fuel efficiency (red) and IPEC device efficiency (blue), the solid and dotted lines denote enthalpy- and Gibbs free energy-based definitions, respectively. **b**, Device current vs voltage. **c**, Fuel power vs DNI. **d**, Heat power vs DNI. For **b**, **c** and **d**, the marker colour denotes the system outlet temperature, and the data have been filtered for steady state (as defined in Supplementary Fig. 10). Simulation results are shown as a dotted black line. For reference, a device current of 50 A corresponds to an EC current density of 1 A cm^{-2} and a PV current density of 8.4 A cm^{-2}.

lower DNI is probably explained by lower heat losses due to a smaller temperature difference between process stream and ambient air temperature. Furthermore, this could also be explained by dynamic effects caused by the thermal inertia of the system leading to spurious heat production during temporarily cloudy periods.

## System dynamics and control strategies

The dynamics of the system during operation were found to be advantageously fast. For example, the startup and shutdown sequences can each be completed in approximately 5 minutes (for example, Supplementary Fig. 15). The system was responsive in recovering from perturbations, such as controlled variable set points and during periods of unstable DNI. Shown in Fig. 4, the response to fluctuations in DNI shows clear hysteresis in the current–voltage curve, which is characteristic of thermally integrated PEC devices as predicted from simulations[27] and observed by Fallisch et al.[5]. A first-order response with time delay was fitted (~9 mins onwards in Fig. 4a), and the time constants were estimated to be 49.8 and 67.3 seconds, with a time delay of 22.3 and 58.8 seconds for EC and output water temperatures, respectively. Furthermore, the synergistic effect of thermal integration is shown as an improvement in both the operating current and voltage when the system returns to steady operating temperatures (that is, green section in Fig. 4). Additionally, the system responds quickly to step changes in flow rate and H$_2$ back-pressure set points, as shown in Supplementary Figs. 13 and 14. Furthermore, the system performance is sensitive to

the dynamics of the two-axis optical tracking mechanism (investigated further in Supplementary Fig. 16), highlighting the importance of accurate solar tracking.

As introduced previously[30], flow-rate control could be employed to stabilize system outputs and device operating temperature in response to changes in input irradiance. Here we investigate not only the stabilizing effect of water flow rate on the output temperature but also the increase in average output temperature while not exceeding safe operating temperatures. This is advantageous as the usefulness of an energy stream is a combination of both total thermal power and the temperature of that heat. To demonstrate this flow-rate control, the set point of the global water flow rate was manually decreased towards the end of the day, leading to a corresponding increase in output temperature (Fig. 5a). This concept can be extended to a continuous control loop system using the steady-state process model by neglecting the system dynamics (which have experimentally been found to be rapid—typical first-order time constants τ < 70 seconds for changes in flow rate and DNI). Two example cases are presented in Fig. 5b: a fixed flow rate and a flow rate varied between 3–5 l min^{-1} to stabilize reactor temperature. Fig. 5b shows that this method is very effective in thermal stabilization and in increasing the output temperature at the start and end of the day. Fuel power output is increased by 0.31%, the thermal power output is decreased by 4.6%, and the average temperature of the system output and EC increased by 1.3 °C and 5.2 °C, respectively, when water flow-rate control is
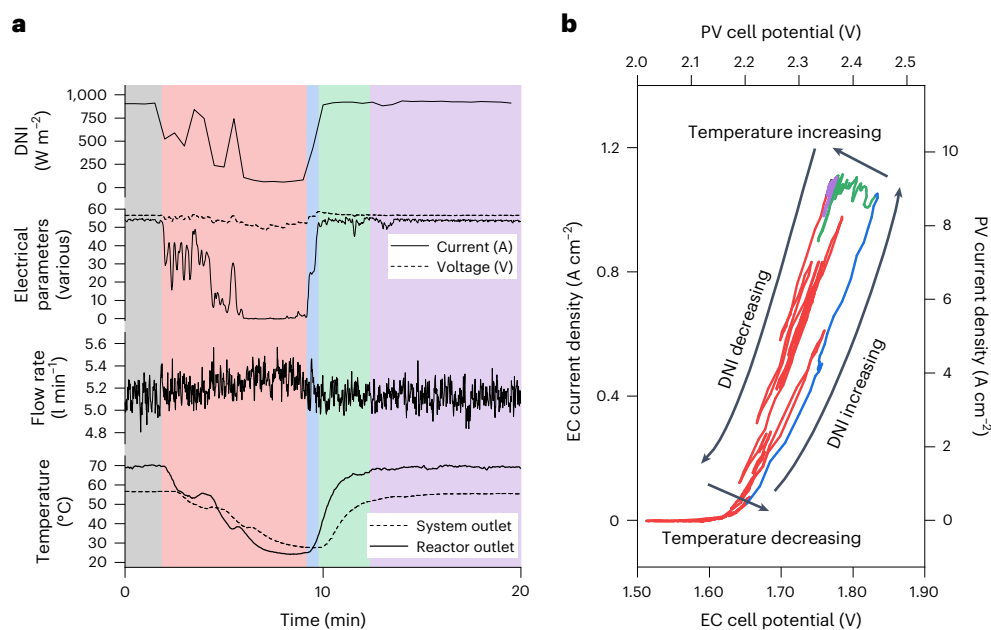
Fig. 4 | Experimental dynamic response to fluctuating DNI (21 August 2020 16:10:00 to 16:30:00). a, Key process variables vs time. **b**, Dynamic position of the current–voltage operating point. Time periods are colour coded to facilitate comparison between changes in process variables and the current–voltage operating point.
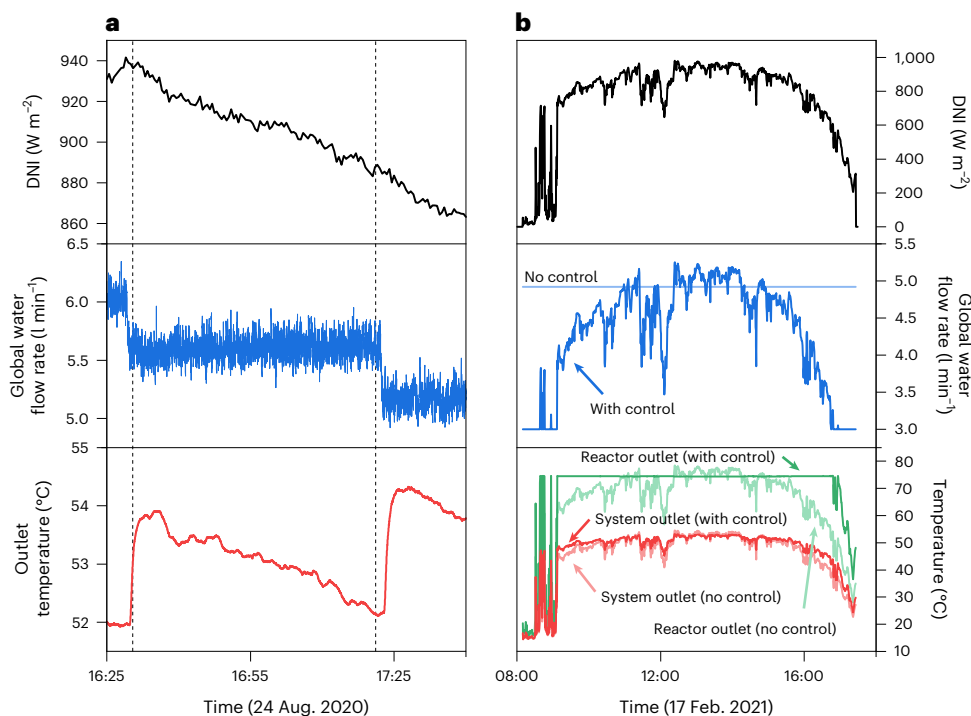

Fig. 5 | Results of water flow-rate control. a, Manual global water flow-rate control to counterbalance the reduction in DNI to stabilize output temperature. Vertical dotted lines indicate a step change to the pump set point. **b**, Simulation results for water flow-rate control stabilizing operating temperatures.

employed. The decrease in thermal output is explained by higher heat losses when outlet temperature is increased, and these heat losses could be largely decreased in future designs with pipe thermal insulation. For example, assuming pipe heat losses are reduced to $UA = \sim 6$ W K^{-1} (UA is the overall heat transfer coefficient multiplied by the heat transfer area). Supplementary Note 9 provides a detailed analysis), the average system output temperature improvement from water flow-rate control increases to 5.0 °C, and the thermal power output is decreased only by 0.22%.

System optimization and outlook

To investigate the energy loss of each sub-component of the integrated system, a Sankey diagram was constructed from averaged data from an example day (Fig. 6) and reasonable estimates as outlined in Supplementary Note 10. This diagram shows that 27.5% of the total solar power reaches the front surface of the PV where the majority of light (52.1%) is reflected/absorbed by the reactor shield and homogenizer. This low overall optical efficiency was inherent in the initial design (that is, oversized solar dish relative to reactor), which aimed to
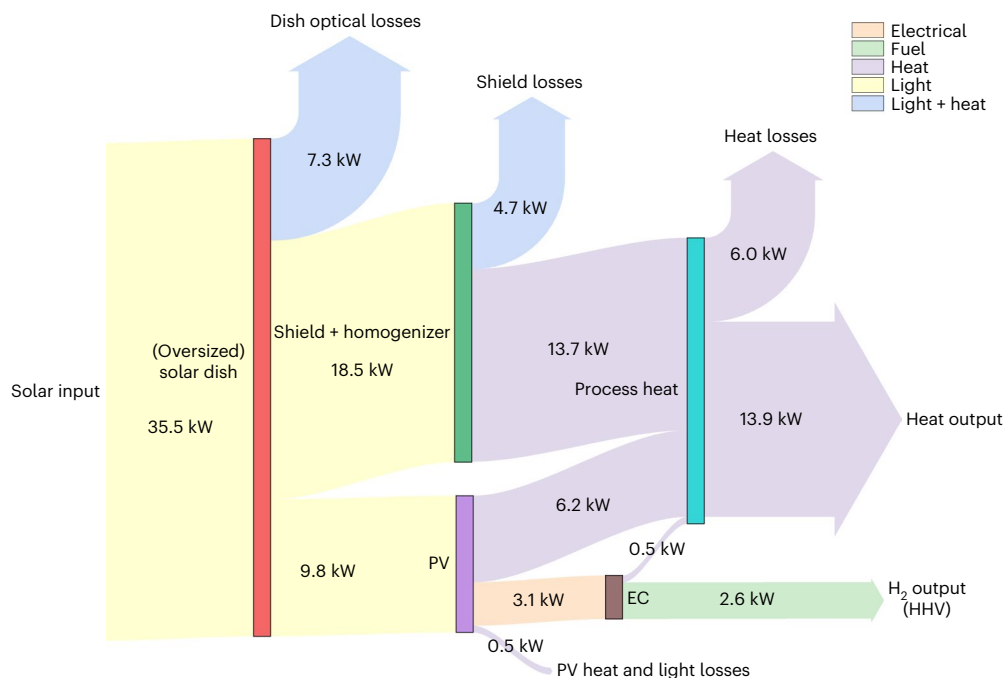
Fig. 6 | Sankey diagram showing the magnitude and routing of the energetic flows through the system. The type of energy is denoted by the arrow colour. Calculated from averaged data (20 August 2020) where reasonable estimates are outlined further in the Supplementary Information (Supplementary Note 10). The external electricity used for all auxiliary components (0.58 kW) is neglected from this diagram.

demonstrate the technology at a kilowatt pilot scale and achieve an improved device-level efficiency compared with previous lab-scale work[3]. System efficiency could be elevated through improved component power matching while still capturing a considerable proportion of the waste PV heat. Additionally, this pipe thermal loss (-15 °C) could easily be reduced through the use of improved pipe insulation.

Using the validated model, a parameter study is used to investigate promising optimization pathways, where key results are shown in Fig. 7. First, increasing the water flow rate leads to marginally lower fuel power due to a reduced short-circuit current (gradient = −0.03 kW (ml min^{-1})$^{-1}$ at 4.9 ml min^{-1}) and increased heat output power as piping heat losses are reduced (1.37 kW (ml min^{-1})$^{-1}$ at 4.9 ml min^{-1}), however with correspondingly colder output temperatures (−4.4 °C (ml min^{-1})$^{-1}$ at 4.9 ml min^{-1}). Secondly, this analysis demonstrates that increasing the fraction of solar power received by the PV module and scaling the PV area accordingly (that is, improved matching of dish power to PV power) and improving the light homogeneity could substantially improve output fuel power (0.09 kW %$^{-1}$ and 0.004 kW %$^{-1}$, respectively) while leading to a comparatively smaller decrease in output heat power (−0.007 kW %$^{-1}$ and −0.002 kW %$^{-1}$, respectively). Finally, in the present configuration, increasing the number of EC cells in the stack would only moderately improve the hydrogen production power (0.04 kW per electrolyser cell at N_{EC} = 32) as it is limited by the light inhomogeneity. This trend continues until ~42 when the performance rapidly deteriorates due to the operating voltage exceeding the voltage at PV maximum power (consistent with the observations in ref. 27).

The optimal system performance can be calculated by taking realistic estimates for feasible improvements for the key optimization parameters identified in the parameter study analysis. If all shield light falls on the PV, the PV area is scaled in proportion (to maintain constant average concentration), and the light homogeneity is 90% improved, the system STH efficiency can be nearly tripled to 15.9% (Gibbs)/19.2% (enthalpy) and improved towards the experimentally achieved device-level STH efficiency of 20.3% (Gibbs)/24.4% (enthalpy). This efficiency can be split into an overall optical efficiency

of 72.6%, a PV light-to-electricity efficiency of 37.3%, an electrolysis efficiency of 59.7% (Gibbs)/71.8% (enthalpy) and a balance-of-plant efficiency of 98.5%. The optimal number of EC cells in the stack was found to be 32 (same as in the current design), and the optimal global mass flow rate was 4.2 l min^{-1}, limited by the maximum PV temperature (100 °C). Hypothetically, the optical efficiency of the solar dish could be improved further still to the state-of-the-art achievable with a high-reflectivity silvered-glass mirror (about 90%) (ref. 41), which would lead to an optimized system STH efficiency of 19.7% (Gibbs)/23.8% (enthalpy). Using a detailed theoretical model outlined in Supplementary Note 9, 20 mm-thick polyethylene foam pipe insulation was added to the piping, and the average heat loss per metre of pipe was reduced to 13.6 W m^{-1} (UA = -6 W K^{-1}). For the theoretically optimized system, this would lead to a 49.3% system heat efficiency with a EC outlet temperature of 81.8 °C and a system outlet temperature of 80.4 °C, compared with the experimental results of 35.8%, ~65 °C and 45.1 °C, respectively. These results are summarized in Supplementary Note 6 alongside a comparison with more conventional solar hydrogen production technology.

In addition to implementing these feasible theoretical improvements, there are multiple avenues for future research. For example, the flexible and simultaneous production of hydrogen, electrical power and heat on demand would be advantageous but will require the study of non-trivial control strategies given the coupled behaviour of the integrated system. Furthermore, as system capacity factor is often key to technological and economic feasibility, it would be promising to investigate the integration with electricity and heat storage technologies to maintain hydrogen production and nominal operating temperatures through periods of fluctuating or low DNI, or to enable 24-hour operation. Further conversion of hydrogen to carbon-based fuels (for example, methanol, kerosene and so on) could be achieved with integration with direct air capture and gas-to-liquid technologies. The technology developed in this work is particularly suited to integration with residential heating or low-temperature industrial process heat (for example, amine sorbent regeneration in amine-based
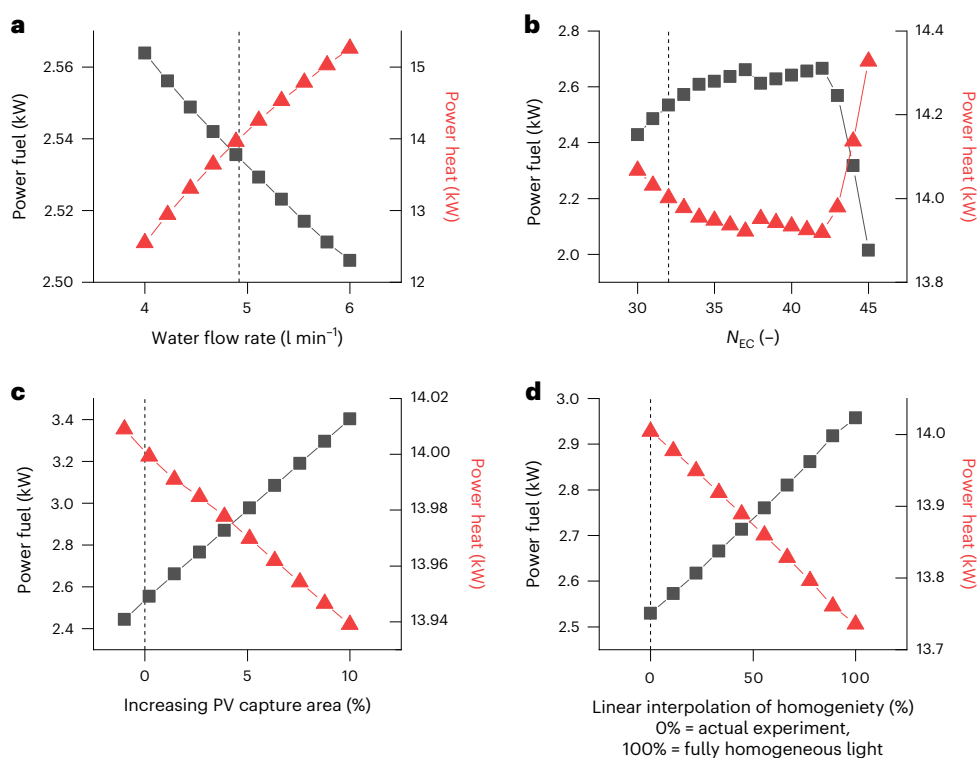
Fig. 7 | Simulations and parametric analysis of fuel power and heat power.
a–d, Simulations of the effect of various parameters on the output fuel power
(left y axis) and heat power (right y axis). **a**, Effect of global water flow rate.
b, Effect of number of electrolysers in series N_{EC}. **c**, Effect of the fraction of solar
power received by the PV module and scaling PV area accordingly. **d**, Effect of
improvements in light homogeneity. For all, the dotted lines indicate the original
values from the experimental demonstration.

direct air capture). Finally, the system presented here should be demonstrated over a multi-year timeframe to substantiate our hypothesis of long-term system stability (for example, PEM stacks now achieve >50,000 h (refs. [36,42])). For example, the effect of intermittent operation on PEM electrolysis is complex and debated but could lead to the reversibility of degradation phenomena[35] and/or catalyst dissolution[43] during periods of open circuit voltage. Therefore, there is potential to investigate control strategies that maintain a small current during non-operation to potentially reduce degradation of the membrane electrode assembly.

Conclusion

In this work, a large-scale (2.97 kW fuel output, 14.9 kW$_{th}$ thermal output at 60 °C and 1.26 g$_{H_2}$ min^{-1} at peak production rate over 5 minutes) and efficient (average 20.3% (Gibbs)/24.4% (enthalpy) device-level STH efficiency, 5.5% (Gibbs)/6.6% (enthalpy) system-level fuel efficiency, 35.3% system-level thermal efficiency) co-generating hydrogen and heat system has been demonstrated on sun. The design and construction of the pilot plant is outlined, highlighting how key non-trivial operational challenges have been overcome, such as the complex process control and judicious management of water flow rates to realize the synergistic effect of thermal integration. The on-sun results demonstrate advantageously fast system dynamics (startup/shutdown takes ~5 minutes) and the successful operation without degradation over various meteorological conditions and ambient temperatures (that is, operation in summer and winter). Controlling strategies were shown to be effective in dampening the solar radiation variation-induced hydrogen and heat-production dynamics. The balance of plant and auxiliary energy losses are comprehensively assessed, which highlight that this device design mitigates the typical requirement for an auxiliary heater for kW-scale electrolysers. A validated model was built to optimize the thermally integrated device and identify facile routes

(that is, scaling PV module area and improving the optics of the homogenizer) to improve system-level performance up to >16% (based on the Gibbs free energy definition). For thermally integrated PV plus EC demonstrations, the hydrogen production rate (>2.0 kW) and average solar concentration level (~800 suns) experimentally achieved in this work represents an encouraging step towards the technological demonstration and commercial realization of such a technology.

Methods

Pilot plant design and operation

The system is shown in a simplified process and instrumentation diagram in Fig. 1c and is explained further here. A 7 m-diameter dual-axis tracking solar parabolic dish (38.5 m^2 collection area) was installed at École Polytechnique Fédérale de Lausanne (EPFL) main campus on a concrete foundation with a covered trench for housing various components and piping. Stainless steel piping and fittings were used for connection of ground-level components, such as upstream components (for example, storage tanks, water pumps, de-ionizers and so on) and downstream components (for example, heat exchangers, water separators, water recycle streams, gas storage tanks and so on). A flexible fluoropolymer-lined tubing was used to make the fluidic connection between the reactor mounted in the focal point of the solar dish and the ground-level components and was routed on a truss of the parabolic dish similar to the electrical and communication cables.

The single continuous feedstock input stream is potable water from the local municipal water supply. The pre-reactor system consists of a water storage tank, a geared water pump, multiple particulate filters and two mixed-bed ion-exchange water deionizers. The water is pumped by the main water pump (this water flow rate is named 'global' from here on) via deionizers to the reactor module. The reactor system contains a concentrator triple-junction solar cell module, two 16-cell PEM electrolyser stacks and a small centrifugal pump that was used to

recycle (re-circulate) water through the concentrated PV module (this stream is named 'PV recycle' from here on). To ensure compatibility of all wetting components with deionized water, as per the the requirements of PEM electrolysis, the wetted surfaces of the concentrated PV module copper heat sink was coated with 50 nm layers of Al_2O_3 and TiO_2 through atomic layer deposition. All other reactor components (for example, shield, homogenizer, enclosure and so on) were custom made. The goal of the water-cooled flux homogenizer is to convert the approximately Gaussian flux profile of the concentrated sunlight coming from the parabolic concentrator to a rectangular (matching the active area of the PV) homogeneous profile using a kaleidoscope-like design. The homogenizer is constructed from a single hollow block of stainless steel cooled by internal water channels, and the inner faces are covered with highly reflective solar mirrors.

The water is heated as it passes through the light homogenizer, concentrated PV and light shield before it is supplied at an elevated temperature to the EC stack. Accordingly, the integrated device achieves photo-driven thermally assisted water splitting as the waste heat generated from the required forced-convection water cooling of the concentrated PV module raises the water temperature (to 30–90 °C dependant on the water flow rate), which improves the EC performance through improvements in catalysis and membrane performance. The resulting anodic (O_2 + unreacted H_2O) and cathodic (H_2 + H_2O by electro-osmotic water drag) streams are transported to ground level.

The product-processing sub-system is comprised of a stainless steel liquid–liquid heat exchanger, custom-made liquid–gas separators (both anodic and cathodic sides) and a back-pressure regulator. The anodic stream is cooled in a liquid–liquid heat exchanger, and then water is removed in the respective liquid–gas separator units and is recycled back to the water storage tank. Hydrogen production pressure is maintained at 1–30 bars by an adjustable back-pressure regulator, and oxygen production is produced at near atmospheric pressure. Finally, the gaseous products are transported to compressed storage 'quads' that are connected to EPFL's mini grid[44] or vented to the atmosphere.

The key parameters such as temperature, pressure, conductivity and flow rates are measured at multiple locations, and an in-line flammable gas sensor calibrated for H_2 ensures avoidance of hazardous product crossover (details on gas crossover in Supplementary Note 2). The operating current and voltage of the integrated device was measured with electrical sensors and the temperatures in the reactor by K-type thermocouples. Inlet and outlet temperatures were measured with a PT100 resistance thermometer. The control cabinet houses various data-acquisition boards, relay control boards, power boards, and a computer (running the control software) for controlling and monitoring data collection from various components and sensors. A supervisory control and data-acquisition system was implemented in LabVIEW programming language (National Instruments) to facilitate automated operation and control of the ~30 valves, ~60 sensors, two pumps and so on. The solar dish movement was controlled by a dedicated programmable logic controller.

Commissioning experiments
The electrical performance of the individual PV and EC components are characterized in situ using a 15 kW bi-directional power supply (Supplementary Figs. 6 and 7). The PV performance was also experimentally tested at 1 Sun in the laboratory and at the manufacturer facility at 700 Suns (Supplementary Table 2).

The optical methodology developed in ref. 45 was applied to determine the spatial distribution of the incident solar radiative flux. The radiative flux measurement system consisted of a 275 × 275 mm² water-cooled custom-made Al_2O_3-plasma-coated Lambertian target, a charge-coupled device camera and a graphite-coated radiative flux gauge (repeatability <3%). The need for a geometric transformation of the raw images[46] was avoided through coaxial camera positioning

with the optical axis of the solar dish. This configuration led to flux map resolution at the target surface of 0.41 mm. Radiative flux maps were taken at varying planes using a custom-built linear stage (positioning precision <1 mm) and were used to assess the optical performance of the system. Further details are provided in Supplementary Methods 1 and Supplementary Figs. 4 and 5.

Integrated experiments and performance metric definitions
A solar irradiance pyranometer was used to continuously monitor the DNI. The startup procedure for the integrated system experiments consist of multiple sequential steps as outlined in Supplementary Fig. 15. The total solar power is defined as $Q_{solar} = DNI \times A_{dish}$. The power of the output fuel is defined as $Q_{fuel} = \frac{I_{EC}N_{EC}\eta_F}{2F} \times \Delta E_{H_2}$ where I_{EC}, N_{EC}, η_F and F are the current, number of cells in series (= 32), Faradaic efficiency (assumed unity) and the Faraday constant, respectively. Depending on the desired efficiency definition, ΔE_{H_2} is either the reaction enthalpy ($\Delta H_{H_2} = 286$ kJ mol^{-1}) or the Gibbs free energy ($\Delta G_{H_2} = 237$ kJ mol^{-1}) of water electrolysis under standard ambient conditions (298.15 K, 1 bar). Finally, the power of the output heat is estimated from $Q_{thermal} = \dot{m}_g C_p (T_{outlet} - T_{inlet})$ where $\dot{m}_g$, C_p, T_{outlet} and T_{inlet} are the global mass flow rate of water, heat capacity, system outlet water temperature and system inlet water temperature (at ground level), respectively. The system fuel and thermal efficiency are defined as: $\eta_{fuel} = Q_{fuel}/(Q_{solar} + Q_{external})$ and $\eta_{thermal} = Q_{thermal}/(Q_{solar} + Q_{external})$, respectively. The diagnostic device efficiency is defined as $\eta_{IPEC} = Q_{fuel}/Q_{PV}$.

Process simulation
A detailed zero-dimensional steady-state model was formulated to simulate the performance of the integrated system (Supplementary Note 8). For each component (that is, solar dish, homogenizer, PV module, shield, electrolyser and piping), energy and mass balance models were constructed with each component connected by material streams and energetic streams (that is, light, heat and electricity). The PV and EC were simulated via a detailed electrical model, which considered non-homogeneity of light flux at the PV surface. Relevant parameters were obtained from literature or fitted to experimental data for optical, component and integrated system performance (Supplementary Table 8).

Data availability
All data supporting the findings in this study are available within the paper and the Supplementary Information. Source data are provided with this paper.

Code availability
The code for the model and the data processing are available for download as Supplementary Code 1.

References
1. Davis, S. J. et al. Net-zero emissions energy systems. *Science* **360**, eaas9793 (2018).
2. Haussener, S. Solar fuel processing: comparative mini-review on research, technology development, and scaling. *Sol. Energy* **246**, 294–300 (2022).
3. Tembhurne, S., Nandjou, F. & Haussener, S. A thermally synergistic photo-electrochemical hydrogen generator operating under concentrated solar irradiation. *Nat. Energy* **4**, 399–407 (2019).
4. Rau, S. et al. Highly efficient solar hydrogen generation—an integrated concept joining III–V solar cells with PEM electrolysis cells. *Energy Technol.* **2**, 43–53 (2014).
5. Fallisch, A. et al. Hydrogen concentrator demonstrator module with 19.8% solar-to-hydrogen conversion efficiency according to the higher heating value. *Int. J. Hydrog. Energy* **42**, 26804–26815 (2017).

6. Fallisch, A. et al. Investigation on PEM water electrolysis cell design and components for a HyCon solar hydrogen generator. *Int. J. Hydrog. Energy* **42**, 13544–13553 (2017).

7. Khan, M. A., Al-Shankiti, I., Ziani, A., Wehbe, N. & Idriss, H. A stable integrated photoelectrochemical reactor for H_2 production from water attains a solar-to-hydrogen efficiency of 18% at 15 Suns and 13% at 207 Suns. *Angew. Chem.* **132**, 14912–14918 (2020).

8. Peharz, G., Dimroth, F. & Wittstadt, U. Solar hydrogen production by water splitting with a conversion efficiency of 18%. *Int. J. Hydrog. Energy* **32**, 3248–3252 (2007).

9. Young, J. L. et al. Direct solar-to-hydrogen conversion via inverted metamorphic multi-junction semiconductor architectures. *Nat. Energy* **2**, 17028 (2017).

10. Ahmet, I. Y. et al. Demonstration of a 50 cm² $BiVO_4$ tandem photoelectrochemical–photovoltaic water splitting device. *Sustainable Energy Fuels* **3**, 2366–2379 (2019).

11. Wang, Q. et al. Scalable water splitting on particulate photocatalyst sheets with a solar-to-hydrogen energy conversion efficiency exceeding 1%. *Nat. Mater.* **15**, 611–615 (2016).

12. Goto, Y. et al. A particulate photocatalyst water-splitting panel for large-scale solar hydrogen generation. *Joule* **2**, 509–520 (2018).

13. Marxer, D., Furler, P., Takacs, M. & Steinfeld, A. Solar thermochemical splitting of CO_2 into separate streams of CO and O_2 with high selectivity, stability, conversion, and efficiency. *Energy Environ. Sci.* **10**, 1142–1149 (2017).

14. Nishiyama, H. et al. Photocatalytic solar hydrogen production from water on a 100-m² scale. *Nature* **598**, 304–307 (2021).

15. Vilanova, A. et al. Solar water splitting under natural concentrated sunlight using a 200 cm² photoelectrochemical–photovoltaic device. *J. Power Sources* **454**, 227890 (2020).

16. Schäppi, R. et al. Drop-in fuels from sunlight and air. *Nature* **601**, 63–68 (2022).

17. Zoller, S. et al. A solar tower fuel plant for the thermochemical production of kerosene from H_2O and CO_2. *Joule* **6**, 1606–1616 (2022).

18. Segev, G. et al. The 2022 solar fuels roadmap. *J. Phys. D: Appl. Phys.* **55**, 323003 (2022).

19. Kim, J. H., Hansora, D., Sharma, P., Jang, J.-W. & Lee, J. S. Toward practical solar hydrogen production—an artificial photosynthetic leaf-to-farm challenge. *Chem. Soc. Rev.* **48**, 1908–1971 (2019).

20. James, B. D., Baum, G. N., Perez, J., Baum, K. N. *Technoeconomic Analysis of Photoelectrochemical (PEC) Hydrogen Production*. Department of Energy contract GS-10F-009J Technical Report (Directed Technologies, 2009).

21. Jia, J. et al. Solar water splitting by photovoltaic-electrolysis with a solar-to-hydrogen efficiency over 30%. *Nat. Commun.* **7**, 13237 (2016).

22. Dumortier, M., Tembhurne, S. & Haussener, S. Holistic design guidelines for solar hydrogen production by photo-electrochemical routes. *Energy Environ. Sci.* **8**, 3614–3628 (2015).

23. Dumortier, M. & Haussener, S. Design guidelines for concentrated photo-electrochemical water splitting devices based on energy and greenhouse gas yield ratios. *Energy Environ. Sci.* **8**, 3069–3082 (2015).

24. Pinaud, B. A. et al. Technical and economic feasibility of centralized facilities for solar hydrogen production via photocatalysis and photoelectrochemistry. *Energy Environ. Sci.* **6**, 1983–2002 (2013).

25. Modestino, M. A. & Haussener, S. An integrated device view on photo-electrochemical solar-hydrogen generation. *Annu. Rev. Chem. Biomol. Eng.* **6**, 13–34 (2015).

26. Wang, Q., Pornrungroj, C., Linley, S. & Reisner, E. Strategies to improve light utilization in solar fuel synthesis. *Nat. Energy* **7**, 13–24 (2022).

27. Holmes-Gentle, I., Tembhurne, S., Suter, C. & Haussener, S. Dynamic system modeling of thermally-integrated concentrated PV-electrolysis. *Int. J. Hydrog. Energy* **46**, 10666–10681 (2021).

28. Segev, G., Beeman, J. W., Greenblatt, J. B. & Sharp, I. D. Hybrid photoelectrochemical and photovoltaic cells for simultaneous production of chemical fuels and electrical power. *Nat. Mater.* **17**, 1115–1121 (2018).

29. Acar, C. & Dincer, I. Enhanced generation of hydrogen, power, and heat with a novel integrated photoelectrochemical system. *Int. J. Hydrog. Energy* **45**, 34666–34678 (2020).

30. Tembhurne, S. & Haussener, S. Controlling strategies to maximize reliability of integrated photo-electrochemical devices exposed to realistic disturbances. *Sustainable Energy Fuels* **3**, 1297–1306 (2019).

31. Briguglio, N. et al. Design and testing of a compact PEM electrolyzer system. *Int. J. Hydrog. Energy* **38**, 11519–11529 (2013).

32. Tembhurne, S. & Haussener, S. Integrated photo-electrochemical solar fuel generators under concentrated irradiation: I. 2-D non-isothermal multi-physics modeling. *J. Electrochem. Soc.* **163**, H988–H998 (2016).

33. Tembhurne, S. & Haussener, S. Integrated photo-electrochemical solar fuel generators under concentrated irradiation: II. thermal management a crucial design consideration. *J. Electrochem. Soc.* **163**, H999–H1007 (2016).

34. Carmo, M., Fritz, D. L., Mergel, J. & Stolten, D. A comprehensive review on PEM water electrolysis. *Int. J. Hydrog. Energy* **38**, 4901–4934 (2013).

35. Rakousky, C. et al. Polymer electrolyte membrane water electrolysis: restraining degradation in the presence of fluctuating power. *J. Power Sources* **342**, 38–47 (2017).

36. Ayers, K. The potential of proton exchange membrane-based electrolysis technology. *Curr. Opin. Electrochem.* **18**, 9–15 (2019).

37. Coridan, R. H. et al. Methods for comparing the performance of energy-conversion systems for use in solar fuels and solar electricity generation. *Energy Environ. Sci.* **8**, 2886–2901 (2015).

38. Becker, J.-P. et al. A modular device for large area integrated photoelectrochemical water-splitting as a versatile tool to evaluate photoabsorbers and catalysts. *J. Mater. Chem. A* **5**, 4818–4826 (2017).

39. Blanc, P. et al. Direct normal irradiance related definitions and applications: the circumsolar issue. *Sol. Energy* **110**, 561–577 (2014).

40. Neumann, A. & Witzke, A. The influence of sunshape on the DLR solar furnace beam. *Sol. Energy* **66**, 447–457 (1999).

41. Buscemi, A., Lo Brano, V., Chiaruzzi, C., Ciulla, G. & Kalogeri, C. A validated energy model of a solar dish-Stirling system considering the cleanliness of mirrors. *Appl. Energy* **260**, 114378 (2020).

42. Schmidt, O. et al. Future cost and performance of water electrolysis: an expert elicitation study. *Int. J. Hydrog. Energy* **42**, 30470–30492 (2017).

43. Weiß, A. et al. Impact of intermittent operation on lifetime and performance of a PEM water electrolyzer. *J. Electrochem. Soc.* **166**, F487–F497 (2019).

44. Belvedere, B. et al. A microcontroller-based power management system for standalone microgrids with hybrid power supply. *IEEE Trans. Sustain. Energy* **3**, 422–431 (2012).

45. Schubnell, M., Keller, J. & Imhof, A. Flux density distribution in the focal region of a solar concentrator system. *J. Sol. Energy Eng.* **113**, 112–116 (1991).

46. Ulmer, S., Reinalter, W., Heller, P., Lüpfert, E. & Martínez, D. Beam characterization and improvement with a flux mapping system for dish concentrators. *J. Sol. Energy Eng.* **124**, 182–188 (2002).

Author contributions

I.H.-G., S.T., C.S. and S.H. conceived and designed the pilot-scale demonstrator. I.H.-G., S.T. and C.S. executed the experiments. I.H.-G. performed the system modelling. S.H. managed and supervised the project. I.H.-G. and S.T. wrote the manuscript with input from all authors.

Competing interests

EPFL has license agreements with its spin-off company: SoHHytec SA. S.H. and S.T. are co-founders and shareholders in SoHHytec SA. I.H.-G. and C.S. declare no competing interests.

Additional information

Supplementary information The online version contains supplementary material available at https://doi.org/10.1038/s41560-023-01247-2.

Correspondence and requests for materials should be addressed to Sophia Haussener.

Peer review information *Nature Energy* thanks Yagya Regmi and the other, anonymous, reviewer(s) for their contribution to the peer review of this work.

Reprints and permissions information is available at www.nature.com/reprints.

Publisher's note Springer Nature remains neutral with regard to jurisdictional claims in published maps and institutional affiliations.